

The diurnal cycle of water ice on comet 67P/Churyumov–Gerasimenko

M. C. De Sanctis¹, F. Capaccioni¹, M. Ciarniello¹, G. Filacchione¹, M. Formisano¹, S. Mottola², A. Raponi¹, F. Tosi¹, D. Bockelée-Morvan³, S. Erard³, C. Leyrat³, B. Schmitt⁴, E. Ammannito^{1,5}, G. Arnold², M. A. Barucci³, M. Combi⁶, M. T. Capria¹, P. Cerroni¹, W.-H. Ip⁷, E. Kuehrt², T. B. McCord⁸, E. Palomba¹, P. Beck⁴, E. Quirico⁴ & the VIRTIS Team*

Observations of cometary nuclei have revealed a very limited amount of surface water ice^{1–7}, which is insufficient to explain the observed water outgassing. This was clearly demonstrated on comet 9P/Tempel 1, where the dust jets (driven by volatiles) were only partially correlated with the exposed ice regions⁸. The observations^{6,7} of 67P/Churyumov–Gerasimenko have revealed that activity has a diurnal variation in intensity arising from changing insolation conditions. It was previously concluded that water vapour was generated in ice-rich subsurface layers with a transport mechanism linked to solar illumination^{1–3,5}, but that has not hitherto been observed. Periodic condensations of water vapour very close to, or on, the surface were suggested^{3,9} to explain short-lived outbursts seen near sunrise on comet 9P/Tempel 1. Here we report observations of water ice on the surface of comet 67P/Churyumov–Gerasimenko, appearing and disappearing in a cyclic pattern that follows local illumination conditions, providing a source of localized activity. This water cycle appears to be an important process in the evolution of the comet, leading to cyclical modification of the relative abundance of water ice on its surface.

The Visible Infrared and Thermal Imaging Spectrometer VIRTIS¹⁰ has collected data of high spatial (7–25 m per pixel) and spectral resolution since the Rosetta spacecraft approached the nucleus of comet 67P/Churyumov–Gerasimenko in August 2014. The reflectance spectra, taken in different areas over the illuminated regions of the comet's nucleus, show a broad absorption band at 2.8–3.6 μm ,

attributed to organic compounds. The absence of pure water ice absorption bands indicates an upper limit of about 1% (by volume) of water ice, in very limited surface regions, at VIRTIS resolution⁴.

Figure 1 shows a small region of the 'neck' (longitude $325^\circ \pm 4^\circ$ E, latitude $31^\circ \pm 5^\circ$ N, called Hapi) of the comet, located between the small and large lobes of the nucleus, observed at different rotational phases after one or more comet rotations. During each rotation, this region moves into the shadows projected by the head (the smaller lobe) bulge. VIRTIS observes variations in the absorption band near 3 μm as this region moves out of the shadow and becomes illuminated (Fig. 2a). In this case we observe a clear alteration of the organic compounds band, with a broadening, a shift towards shorter wavelengths and a strong increase in depth with decreasing illumination. The band centre shifts from $3.22 \pm 0.05 \mu\text{m}$ to $3.12 \pm 0.05 \mu\text{m}$, its short-wavelength shoulder shifts from $2.82 \pm 0.05 \mu\text{m}$ to $2.71 \pm 0.05 \mu\text{m}$, and the band depth relative to the continuum increases from 0.20 ± 0.03 to 0.60 ± 0.03 . We also observe a flattening of the continuum slope and a reduced thermal emission as the 3- μm band depth increases.

The stronger 3- μm band and the flattening of the continuum suggest exposed water ice, in addition to the organic material ubiquitously present on the comet's surface⁴. The spectral ratio (Fig. 2) between the spectrum of a pixel close to the shadow and the spectrum of an illuminated pixel shows the presence of a strong ice band extending from 2.7 μm to 3.6 μm , while the other water ice bands at 1.5 μm and 2.0 μm are not detected¹¹ (see Extended Data Fig. 1). The 3- μm water band is

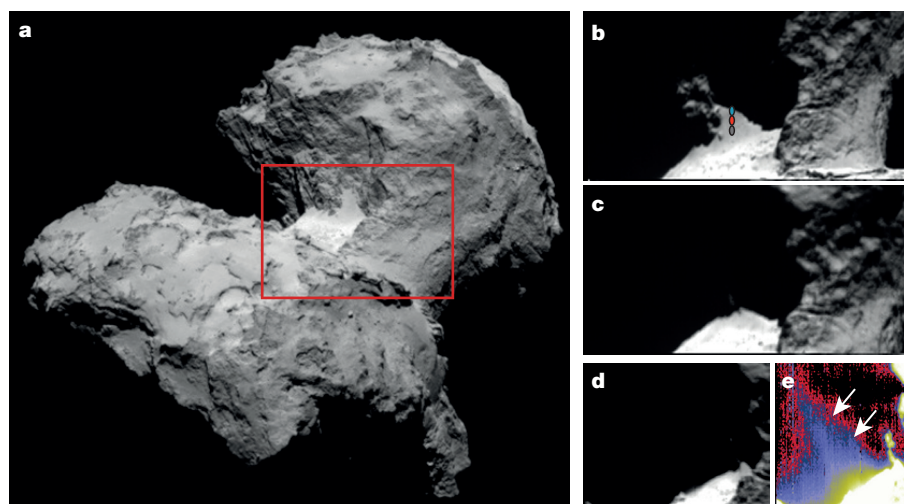


Figure 1 | Images of the ice-rich area. **a**, Rosetta Optical Navigation Camera (OPNAV) context image of the region under study (red box); **b–e**, VIRTIS image at 0.7 μm of the region in the red box of **a**. The data in **b**, **c** and **d** were acquired on 12, 13 and 14 September 2014, respectively. The VIRTIS data in **b** and **c** are separated by ~ 12 h, corresponding to ~ 1 comet rotation, while the data in **c** and **d** are separated by 37.3 h, corresponding to ~ 3 comet rotations. The coloured dots in **b** indicate the zones from which the spectra in Fig. 2 are taken. Panel **e** is the same as **d**, but stretched to see the jet (white arrows).

¹Istituto di Astrofisica e Planetologia Spaziali – INAF, via del fosso del cavaliere 100, 00133 Rome, Italy. ²Institute for Planetary Research, DLR, Rutherfordstraße 2, 12489 Berlin, Germany. ³LESIA-Observatoire de Paris, CNRS, Université Pierre et Marie Curie, Université Paris Diderot, 5 place Jules Janssen, 92195 Meudon, France. ⁴Université Grenoble Alpes – CNRS Institut de Planetologie et Astrophysique de Grenoble, Batiment D de Physique, BP 53, 38041 Grenoble Cedex 9, France. ⁵University of California, Los Angeles, California 90095, USA. ⁶Department of Atmospheric, Oceanic and Space Sciences, University of Michigan, 2455 Hayward Street, Ann Arbor, Michigan 48109, USA. ⁷National Central University, No. 300, Jhongda Road, Jhongli District, Taoyuan City, 32001 Taipei, Taiwan. ⁸Bear Fight Institute, 22 Fiddler's Road, Box 667, Winthrop, Washington 98862, USA.

*A list of participants and their affiliations is given at the end of this paper.

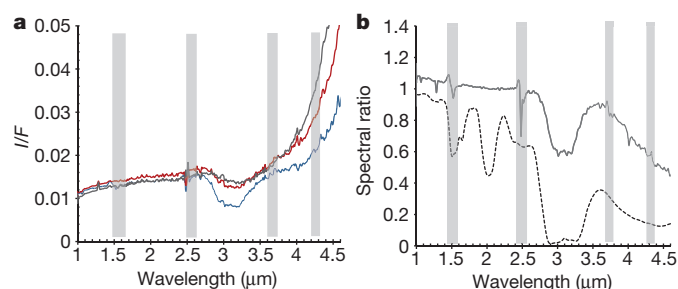


Figure 2 | Spectra of the ice-rich areas. **a**, Spectra from Fig. 1b going from illuminated pixels to shadow. Black, red and cyan spots in Fig. 1b correspond to black, red and cyan spectra, respectively, taken at steps of 1 pixel. At wavelengths >3.5 – $3.7\ \mu\text{m}$, the spectra show smaller thermal emission for the pixels closer to the shadow line. The retrieved temperatures are $175 \pm 8\ \text{K}$, $184 \pm 5\ \text{K}$ and $195 \pm 4\ \text{K}$ for the cyan, red and black spots, respectively. **b**, Spectral ratio of the cyan and black spectrum of **a** (solid line) and a synthetic spectrum of water¹¹ (grain size of $10\ \mu\text{m}$, dashed line). Instrument filters are indicated by grey bars.

clearly present in all the pixels located at the border of the shadowed region. The same region has been observed again one and four nucleus revolutions¹² later (Fig. 1b–d) under slightly different illumination conditions, as shown by the shadows which cover different areas. Nevertheless, in each observation, the presence and change in the

water absorption band depth is controlled by the shadow location and not by the specific surface region. VIRTIS observes areas in which the spectra display progressive $3\text{-}\mu\text{m}$ band weakening as the region moves into greater illumination. Shadowed areas are slightly different from the illuminated regions in the VIRTIS observations (Fig. 1b–d), and ice-rich and ice-free pixels change according to their distance from the shadow: ice-free pixels in the first observation (Fig. 1b) show the ice signature ('ice-rich') on the following observation (Fig. 1c, d) where they are now closer to the shadow.

Using optical constants^{13–16} and scattering theory¹⁷, we modelled the spectra as an intimate mixture of ice and a dark non-ice component (Methods, Extended Data Figs 1 and 2) and derived water-ice abundance maps (Fig. 3). The fit of the spectra requires a relative abundance of up to 10–15% of water ice intimately mixed with the non-ice component, as shown in the ice distribution maps (Fig. 3a). The maps indicate that the maximum quantity of ice is found very close to the shadows in all the observations, even if the pixels close to the shadows are at a different location on the comet surface.

The spectra also show differences at wavelengths longer than $3.6\ \mu\text{m}$, owing to variations of the thermal emission as the region moves into reduced solar illumination, with a correlation of a stronger $3\text{-}\mu\text{m}$ band with a weaker thermal emission, thus with lower temperatures. The nucleus surface temperatures were retrieved from the long-wavelength portion ($>4.5\ \mu\text{m}$) of the VIRTIS spectra¹⁸. The temperatures retrieved for the pixels near the shadows are at most $160\ \text{K}$ with an uncertainty of

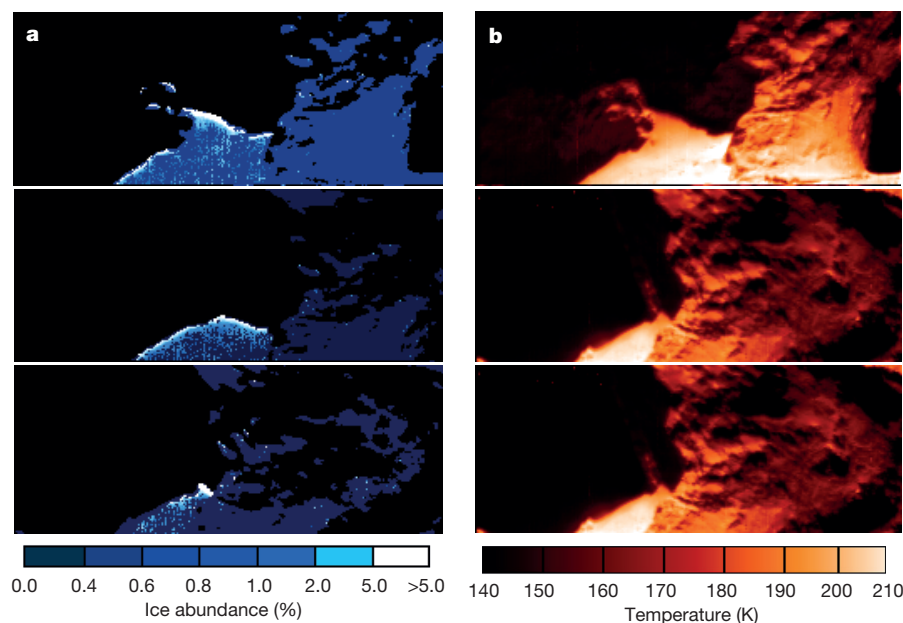
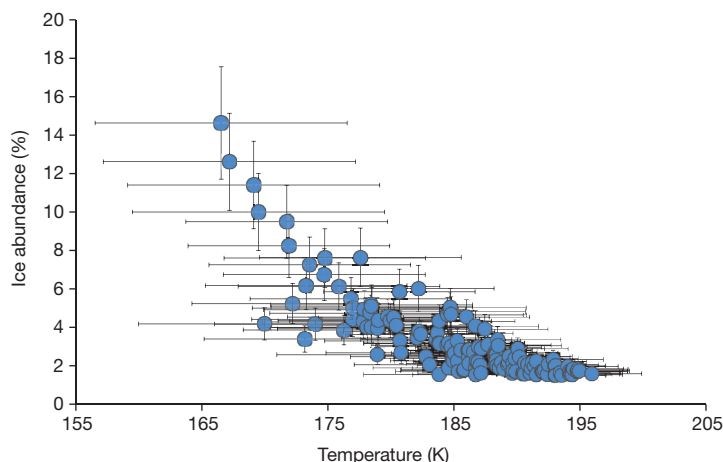


Figure 3 | Ice and temperature maps. **a**, Ice maps: ice abundance (by volume) as shown by the colour scale under. The black pixels are those in shadow or corresponding to sky. Isolated bright pixels are due to instrumental artefacts. **b**, Temperature images. White colours correspond to high temperatures while red-brown colours correspond to low temperatures (see colour scale under). **c**, Scatter plot of ice abundance versus temperature. The data points are extracted from **a** and refer to the region of the neck near the shadow. The error associated with the ice amount is 20%, and errors on the temperatures are $\sim 3\%$ above $170\ \text{K}$ and $\sim 5\%$ below $170\ \text{K}$.



± 10 K, while the temperature of the well illuminated areas are up to 210 K with an uncertainty of ± 2 K (Fig. 3b). The pixels showing the strongest 3- μm absorption have temperatures in the range 160–180 K and a derived ice content varying in a range between $5 \pm 1\%$ and $14 \pm 3\%$ (Fig. 3). The measured temperatures for these pixels are consistent with the presence of water ice in the nucleus outer layers. Water ice sublimation pressure¹⁹ varies by three orders of magnitude from temperatures in the shadowed areas (< 1 nbar), to temperatures in the illuminated areas, where the activity occurs. A clear anti-correlation of ice abundance with temperatures is seen (Fig. 3c) in the regions near the shadows of Fig. 1b, indicating that the temperature is cold enough to maintain ice at, or near, the surface in the shadows.

Most of the activity observed in the period August–September 2014 is from the comet neck^{6,7}, where the region previously examined is located (Fig. 1a). Activity from this specific region is seen in all the data presented here, especially in the data acquired last (Fig. 1e), indicating that a source of water exists to sustain the flux. The amount of water flux coming from the superficial ice documented by VIRTIS represents $\sim 3\%$ of the total water flux measured by MIRO⁶ (see Methods for calculations). From this, we can extrapolate that a much larger area is affected by the same mechanism (although this larger area is not directly observed) and is thus contributing to a larger amount of total water flux. Indeed, all the Hapi region is subjected to this diurnal shadowing effect which can lead to the outgassing over much larger areas. It must be mentioned that the contribution to the total outgassing from these surface layers sources is limited in time. This is demonstrated by the progressive decrease of the abundance of deposited water ice in pixels exposed for a longer time to the solar illumination (see Fig. 3). In the case studied here, the presence of surface ice close to the location of the jets indicates that the outgassing source is likely to be in the uppermost layers of the surface.

The above description of VIRTIS observations of ice sublimating in this neck region (Hapi) when an area emerges from shadow, and the progressive decrease of the ice abundance away from the shadow, clearly indicates that a cyclic sublimation–condensation process is at work during each comet rotation.

Two possible mechanisms for the cyclic condensation of water on unilluminated areas can be considered: (1) the condensation of water vapour present in the coma, and/or redeposition of icy grains, on cold areas on the nucleus^{20,21}, or (2) the direct condensation of gas sublimating from the subsurface under appropriate thermodynamic conditions^{9,22–24}. The first case could indeed occur in the region of the neck where, because of the large concavity, sublimated molecules from an illuminated region could impact and condense on nearby non-illuminated areas. However, this mechanism seems to be more efficient at small heliocentric distance when gas production rate is high enough to enhance the re-deposited flux significantly²⁰. The second mechanism has been already suggested to explain the outbursts observed by the Deep Impact mission on comet 9P/Tempel 1 that appear to occur near sunrise on a particular area⁹, while extensive subsurface sources were invoked to explain the overall ambient outgassing as the observed area of exposed pure ice has a too-limited extent². In addition, during the fly-by of 103P/Hartley 2, the DIXI mission has revealed surface ice notably only along the morning terminator, suggesting diurnal effects²⁵.

The VIRTIS observations are now able to demonstrate that a mechanism similar to (2) above is at work; our thermo-physical model of the nucleus, along with previous literature^{9,22,24}, enables the diurnal cycle of water to be quantified. When the surface is illuminated, water ice sublimates mainly from the uppermost surface layers (Fig. 4 and Extended Data Figs 3 and 4). When the surface goes into shadow (or into the night side), a temperature inversion occurs between the now colder surface layer and the interior layers which maintain a higher temperature for a longer time; the magnitude of this process is controlled by the duration of the shadow/night period and by the thermal inertia of the material and extends to a depth defined by the thermal skin depth. In the present case, the thermal inertia is constrained by

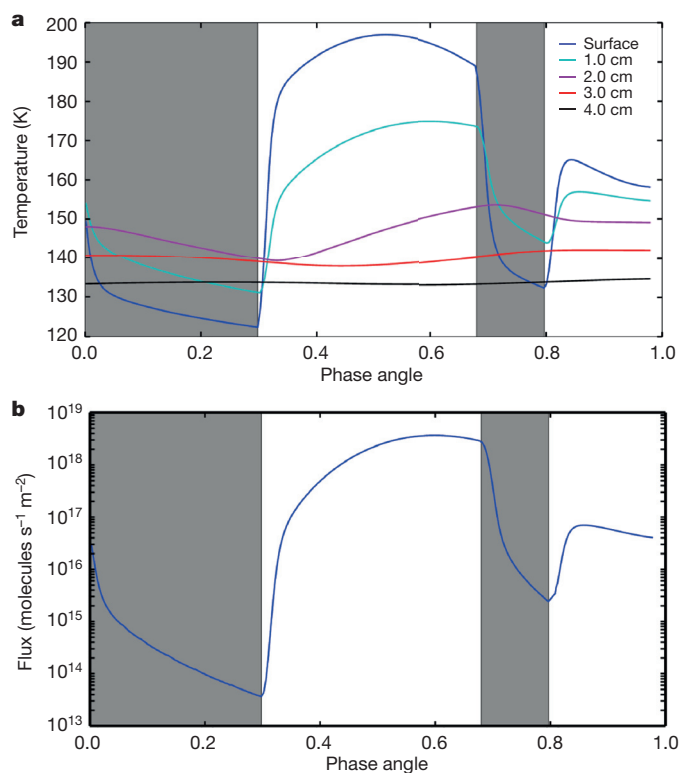


Figure 4 | Temperature and water vapour versus time. **a**, Simulated temperature at different depths from the nucleus surface to the interior (see key at right), over one rotational period, for a small region of the neck near the shadows. **b**, Simulated flux of water vapour versus time over one rotational period. The simulation has been done using the ‘Rome’ model^{22,24} (Methods) and the parameters reported in Extended Data Table 2. The grey bars correspond to unilluminated periods of time due to the combination of comet rotation and shadows.

independent measurements^{4,6} and gives rise to a thermal skin depth of the order of few centimetres (Fig. 4 and Extended Data Fig. 4).

Thus, within the few centimetres affected by the heat exchange, water vapour still produced by subsurface sublimation in the warmer subsurface layers flows through the pores and could re-condense if the thermo-physical conditions of the colder upper surface layer allow it. By this mechanism the surface layer becomes enriched in water ice. The water ice in the uppermost surface layers will be stable until a new cycle of solar illumination starts which will increase the surface temperature and thus trigger again the outgassing of water from the comet (Extended Data Fig. 3).

We thus suggest that the cyclic sublimation–condensation of ice triggered by varying illumination conditions is a general process acting on cometary nuclei. This process implies the cyclical modification of the relative abundance of water ice on the surface of the comet, contributing to the local water activity. This mechanism could lead to differential erosion of the surface, producing morphological differences or enhancing prior existing inhomogeneities. This mechanism could also contribute to activity arising from the pits on comet 67P/Churyumov–Gerasimenko²⁶, being relevant to the shadowing effects in the pits.

Moreover, the surface erosion of 67P/Churyumov–Gerasimenko could keep the water ice close to the surface, thus avoiding fading of activity with time. Finally, as this comet moves towards its perihelion, which will be reached in August 2015, the solar radiation will increase with the inverse square of the heliocentric distance, and thus this process of water sublimation–condensation will become progressively more energetic, possibly leading to the formation of outbursts events like those observed on the nucleus of 9P/Tempel 1.

Online Content Methods, along with any additional Extended Data display items and Source Data, are available in the online version of the paper; references unique to these sections appear only in the online paper.

Received 25 April; accepted 19 June 2015.

- Soderblom, L. A. *et al.* Observations of Comet 19P/Borrelly by the miniature integrated camera and spectrometer aboard Deep Space 1. *Science* **296**, 1087–1091 (2002).
- Sunshine, J. M. *et al.* Exposed water ice deposits on the surface of comet 9P/Tempel 1. *Science* **311**, 1453–1455 (2006).
- A'Hearn, M. F. *et al.* EPOXI at comet Hartley 2. *Science* **332**, 1396–1400 (2011).
- Capaccioni, F. *et al.* The organic-rich surface of comet 67P/Churyumov-Gerasimenko as seen by VIRTIS/Rosetta. *Science* **347**, <http://dx.doi.org/10.1126/science.aaa0628> (2015).
- Feaga, L. M. *et al.* Asymmetries in the distribution of H₂O and CO₂ in the inner coma of Comet 9P/Tempel 1 as observed by Deep Impact. *Icarus* **190**, 345–356 (2007).
- Gulkis, S. *et al.* Subsurface properties and early activity of comet 67P/Churyumov-Gerasimenko. *Science* **347**, <http://dx.doi.org/10.1126/science.aaa0709> (2015).
- Sierk, H. *et al.* On the nucleus structure and activity of comet 67P/Churyumov-Gerasimenko. *Science* **347**, <http://dx.doi.org/10.1126/science.aaa1044> (2015).
- Farnham, T. L. *et al.* Dust coma morphology in the Deep Impact images of Comet 9P/Tempel 1. *Icarus* **191**, 146–160 (2007).
- Prialnik, D., A'Hearn, M. F. & Meech, K. J. A mechanism for short-lived cometary outbursts at sunrise as observed by Deep Impact on 9P/Tempel 1. *Mon. Not. R. Astron. Soc.* **388**, L20–L23 (2008).
- Coradini, A. *et al.* An imaging spectrometer for the Rosetta mission. *Space Sci. Rev.* **128**, 529–559 (2007).
- Filacchione, G. *et al.* Saturn's icy satellites and rings investigated by Cassini-VIMS: III — Radial compositional variability. *Icarus* **220**, 1064–1096 (2012).
- Mottola, S. *et al.* The rotation state of 67P/Churyumov-Gerasimenko from approach observations with the OSIRIS cameras on Rosetta. *Astron. Astrophys.* **569**, L2 (2014).
- Warren, S. G. Optical constants of ice from the ultraviolet to the microwave. *Appl. Opt.* **23**, 1206–1225 (1984).
- Mastrapa, R. M. *et al.* Optical constants of amorphous and crystalline H₂O-ice in the near infrared from 1.1 to 2.6 μm . *Icarus* **197**, 307–320 (2008).
- Mastrapa, R. M. *et al.* Optical constants of amorphous and crystalline H₂O-ice: 2.5–22 μm (4000–455 cm^{-1}) optical constants of H₂O-ice. *Astrophys. J.* **701**, 1347–1356 (2009).
- Clark, R. N. *et al.* The surface composition of Iapetus: mapping results from Cassini VIMS. *Icarus* **218**, 831–860 (2012).
- Hapke, B. *Theory of Reflectance and Emittance Spectroscopy* (Cambridge Univ. Press, 2012).
- Tosi, F. *et al.* Thermal measurements of dark and bright surface features on Vesta as derived from Dawn/VIR. *Icarus* **240**, 36–57 (2014).
- Fray, N. & Schmitt, B. Sublimation of ices of astrophysical interest: a bibliographic review. *Planet. Space Sci.* **57**, 2053–2080 (2009).
- Rubin, M. *et al.* Mass transport around comets and its impact on the seasonal differences in water production rates. *Astrophys. J.* **788**, 168 (2014).
- Crifo, J. F., Loukianov, G. A., Rodionov, A. V. & Zakharov, V. V. Navier-Stokes and direct Monte Carlo simulations of the circumnuclear coma II. Homogeneous, aspherical sources. *Icarus* **163**, 479–503 (2003).
- De Sanctis, M. C., Lasue, J. & Capria, M. T. Seasonal effects on comet nuclei evolution: activity, internal structure, and dust mantle formation. *Astron. J.* **140**, 1–13 (2010).
- Rosenberg, E. D. & Prialnik, D. The effect of internal inhomogeneity on the activity of comet nuclei — application to Comet 67P/Churyumov-Gerasimenko. *Icarus* **209**, 753–765 (2010).
- De Sanctis, M. C. *et al.* Shape and obliquity effects on the thermal evolution of the Rosetta target 67P/Churyumov-Gerasimenko cometary nucleus. *Icarus* **207**, 341–358 (2010).
- Sunshine, J. M. *et al.* Water ice on comet 103P/Hartley 2. *EPSC-DPS Joint Meeting 2011*, 1345 (2011); available at <http://meetingorganizer.copernicus.org/EPSC-DPS2011/EPSC-DPS2011-1345.pdf>.
- Vincent, J. B. *et al.* Large heterogeneities in comet 67P as revealed by active pits from sinkhole collapse. *Nature* **523**, 63–66 (2015).

Acknowledgements We thank the following institutions and agencies, which supported this work: the Italian Space Agency (ASI, Italy), Centre National d'Etudes Spatiales (CNES, France), Deutsches Zentrum für Luft- und Raumfahrt (DLR, Germany), and the National Aeronautic and Space Administration (NASA, USA). VIRTIS was built by a consortium from Italy, France and Germany, under the scientific responsibility of the Istituto di Astrofisica e Planetologia Spaziali of the INAF (Italy), which also guides the scientific operations. The VIRTIS instrument development for ESA has been funded and managed by ASI, with contributions from Observatoire de Meudon financed by CNES (France), and from DLR (Germany). We also thank the Rosetta Science Ground Segment and the Rosetta Mission Operations. The VIRTIS calibrated data will be available through the ESA's Planetary Science Archive (PSA) website.

Author Contributions M.C.D.S. and F.C. contributed to data analysis and the writing of the manuscript. G.F. and F.C. provided calibrated VIRTIS data. A.R. and M.C. provided the spectral fit. M.C.D.S., M.T.C., M.F. and S.T. provided the thermal modelling. F.T. retrieved the temperatures. All authors contributed to the discussion of the results and to the writing of the paper.

Author Information Reprints and permissions information is available at www.nature.com/reprints. The authors declare no competing financial interests. Readers are welcome to comment on the online version of the paper. Correspondence and requests for materials should be addressed to M.C.D.S. (mariacristina.desanctis@iaps.inaf.it)

The VIRTIS Team

G. Piccioni¹, G. Bellucci¹, M. Fulchignoni², R. Jaumann³, K. Stephan³, A. Longobardo¹, V. Mennella⁴, A. Migliorini¹, J. Benkhoff⁵, J. P. Bibring⁶, A. Blanco⁷, M. Blecka⁸, R. Carlson⁹, U. Carsenty³, L. Colangeli³, M. Combes², J. Crovisier², P. Drossart², T. Encrenaz², C. Federico¹⁰, U. Fink¹¹, S. Fonti⁷, P. Irwin¹², Y. Langevin⁶, G. Magni¹, L. Moroz³, V. Orofino⁷, U. Schade¹³, F. Taylor¹², D. Tiphene², G. P. Tozzi¹⁴, N. Biver², L. Bonal¹⁵, J.-Ph. Combe¹⁶, D. Despan², E. Flamini¹⁷, S. Fornasier², A. Frigeri¹, D. Grassi¹, M. S. Gudipati⁹, F. Mancarella⁹, K. Markus³, F. Merlin², R. Orosei¹⁸, G. Rinaldi¹, M. Cartacci¹, A. Cicchetti¹, S. Giuppi¹, Y. Hello², F. Henry², S. Jacquino², J. M. Reess², R. Noschese¹, R. Politi¹ & G. Peter³

¹INAF-IAPS, Istituto di Astrofisica e Planetologia Spaziali, 00133 Rome, Italy. ²LESIA, Observatoire de Paris/CNRS/UPMC/Université Paris-Diderot, 92195 Meudon, France. ³Institute for Planetary Research, DLR, 12498 Berlin, Germany. ⁴Osservatorio di Capodimonte, 80131 Napoli, Italy. ⁵European Space Agency – ESTEC, 2201 AZ, The Netherlands. ⁶Institut d'Astrophysique Spatiale CNRS, 91400 Orsay, France. ⁷Dipartimento di Matematica e Fisica "Ennio De Giorgi", Università del Salento, 73100, Lecce, Italy. ⁸Space Research Centre, Polish Academy of Sciences, 00-716 Warsaw, Poland. ⁹NASA JPL, Pasadena, California 91109, USA. ¹⁰Università di Perugia, 06123 Perugia, Italy. ¹¹Lunar Planetary Laboratory, University of Arizona, Tucson, Arizona 85721, USA. ¹²Department of Physics, Oxford University, Oxford OX1 3RH, UK. ¹³Helmholtz-Zentrum Berlin für Materialien und Energie, 14109 Berlin, Germany. ¹⁴Osservatorio Astrofisico di Arcetri, 50125, Firenze, Italy. ¹⁵Université Grenoble Alpes – CNRS Institut de Planetologie et Astrophysique de Grenoble, Batiment D de Physique, BP 53, 38041 Grenoble Cedex 9, France. ¹⁶Bear Fight Institute, Winthrop, Washington 98862, USA. ¹⁷Agenzia Spaziale Italiana, 00133 Rome, Italy. ¹⁸Istituto di Radioastronomia – INAF, 40129 Bologna, Italy.

METHODS

Data. VIRTIS observations were acquired in September 2014 when the Rosetta spacecraft was orbiting at a distance of about 27 km from comet 67P/Churyumov–Gerasimenko’s surface resulting in a spatial resolution on the ground of about 7 m per pixel. During this period the instrument was observing the morning hemisphere with a solar phase of about 60–70°. VIRTIS-M-IR data were acquired in scan mode with an integration time of 3 s. The characteristics of the data here used are reported in Extended Data Table 1.

Spectral modelling. In order to model nucleus surface spectra, a solution of the radiative transfer equation in a particulate medium must be applied. In this paper we adopt the Hapke model¹⁷. Our analysis is performed on normalized spectra in order to rule out the effect of surface roughness and minimize photometric issues. We model the icy regions of the comet, following the equations below, as formed by a two end-members regolith made of a ‘dark terrain’ (DT) and water ice. The DT represents the average spectrum of the comet surface after photometric correction. Water ice is modelled as in ref. 27, starting from optical constants which are obtained from refs 13–16 to cover the VIRTIS wavelength range.

We investigated two mixing modalities: areal and intimate. Areal mixtures are obtained from a linear combination of the reflectances (r) of water ice and DT:

$$r_{\text{eff}} = fr_{\text{H}_2\text{O}} + (1-f)r_{\text{DT}} \quad (1)$$

where f is the relative amount of water ice and r_{eff} is the effective reflectance of the medium. Intimate mixture (‘salt and pepper’) is modelled as a linear combination of the two end-members single scattering albedoes (w) and is given by:

$$w_{\text{eff}} = fw_{\text{H}_2\text{O}} + (1-f)w_{\text{DT}} \quad (2)$$

where the derived w_{eff} is used to compute the final reflectance. In both cases, along with the amount of water, the grain diameter d is also retrieved.

The modelling of the observed spectra is performed by a retrieval procedure that searches for the minimum of the reduced chi-square (χ^2_{R}), namely the best fit between the modelled (r^m) and the observed (r^o) reflectance:

$$\chi^2_{\text{R}} = \sum_{j=1}^N \left(\frac{r_j^o - r_j^m}{\sigma_j} \right)^2 \frac{1}{\text{DOF}} \quad (3)$$

where j identifies each band (λ), N is the total number of bands, DOF are the degrees of freedom.

The observed spectra are corrected for spikes and instrumental artefacts. Among the residual sources of error, like stray light and signal from the coma, instrumental noise is the main contribution to the error of the measured reflectance (σ_j).

In Extended Data Fig. 1 we report, as an example, the result of a typical spectral fit for a pixel exhibiting a certain amount of ice obtained in the intimate and the areal modes. It can be noted that intimate mixing provides the best match with measured spectra. The reason is that areal mixing increases the relative depth of 1.5- μm and

2- μm absorption bands with respect to the 3- μm feature, while they are very weak or absent across the data set investigated in this work. Given this, the water ice abundance maps are obtained modelling the spectra as intimate mixtures.

The non-detection of the water ice bands at 1.5 μm and 2.0 μm indicates that the water ice and non-icy components are intimately mixed. In fact an areal mixture of 1% of water ice and 99% of non-ice materials also yields spectra with well-defined absorption features at 1.5 and 2 μm as well as an increase in reflectance (Extended Data Fig. 1). This was the case with comet 9P/Tempel 1, where ice-rich patches on the nucleus have been modelled through an areal mixture containing $6 \pm 3\%$ ice².

The maps showing the abundance of water ice (Fig. 3) are produced by setting a threshold of 50 on the median S/N of the spectra in order to avoid pixels in shadow or not of the nucleus of the comet.

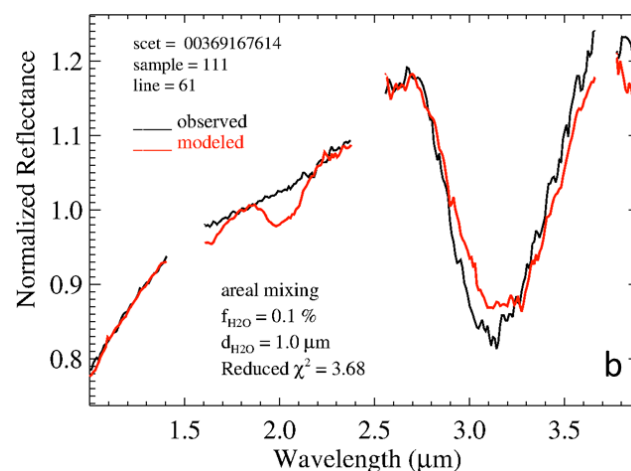
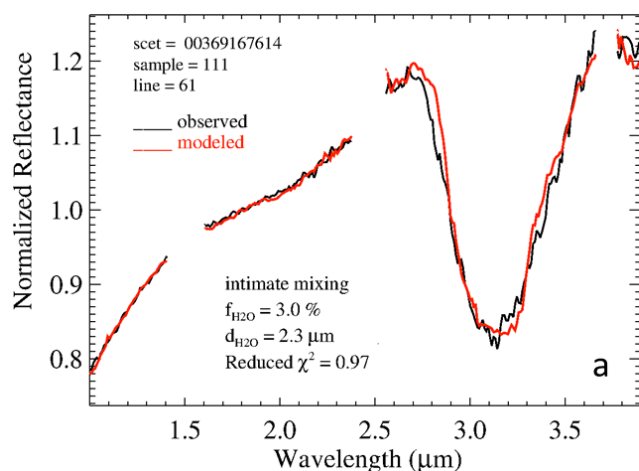
In Extended Data Fig. 2, we report the spectra of three consecutive pixels going out of the shadow, and thus with decreasing abundance of water ice. The relative accuracy of the parameters obtained from the spectral modelling (water ice amount and grain diameter) is of the order of 20%, due to the instrumental noise and the uncertainty on the level of the dark terrain.

Estimation of water flux. The contribution to the total outgassing was estimated using only the extent of ice in our data. We calculated the surface area in the data that contains the transient ice and the percentage of ice in such an area. Using that information, and the pixel size, we computed the equivalent area covered by pure ice. In the VIR data, this area is $\sim 1 \text{ km}^2$.

MIRO measured about 10^{25} molecules s^{-1} and they estimated that between 0.1 and 1% of the 67P nucleus surface is needed to explain the water gas production rates if water ice were located on the surface⁶. Thus, using these values we can say that the ‘transient ice’ seen by VIRTIS contributed $\sim 3\%$ to the total water flux. However, this is the lower limit of the contribution. In fact we can extrapolate that a similar fraction of the neck region, even if not observed by VIR due to observation conditions, is subject to a similar diurnal illumination effect and could have ice deposits like the imaged area.

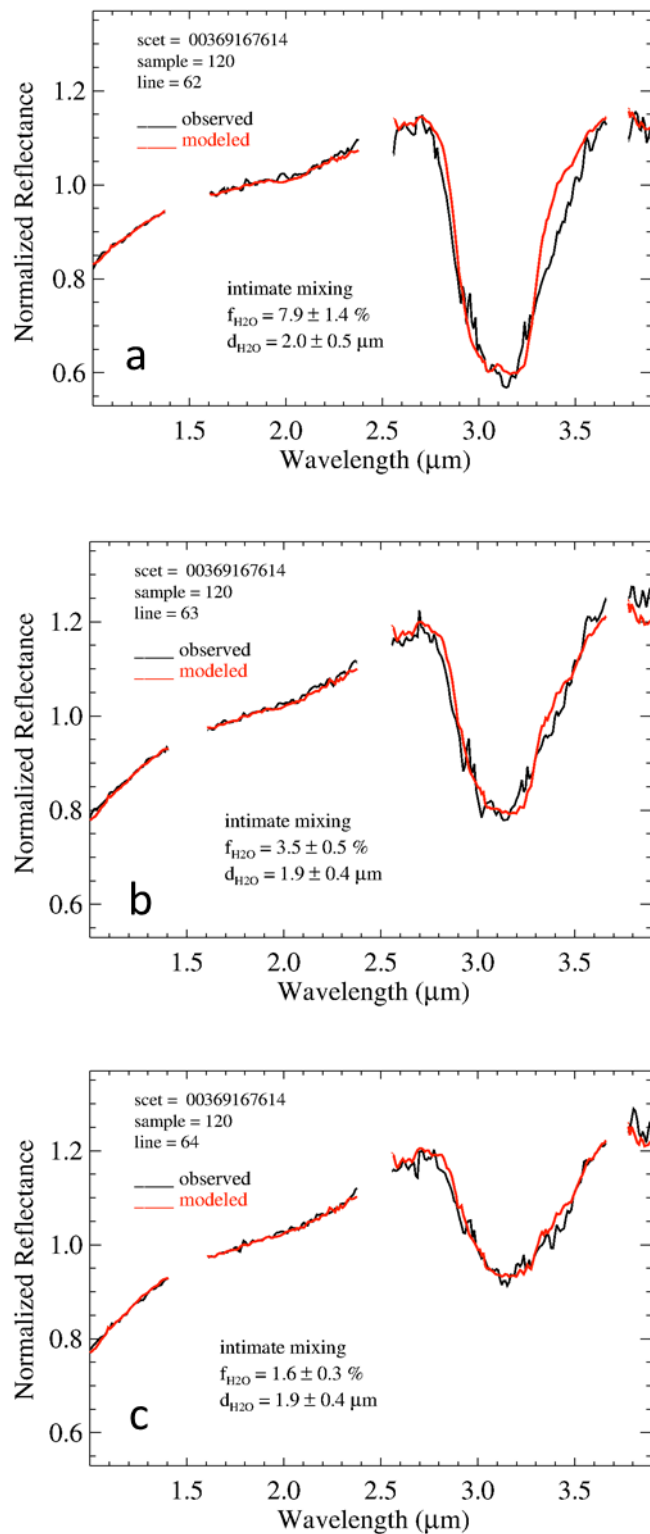
Code availability. The code used to generate the thermal models of comet 67P is a direct implementation of a published model^{24,28,29}. The code used to generate the spectral fit is described above. The code used to retrieve the nucleus temperatures of comet 67P is a direct implementation of a published method¹⁸.

27. Ciarniello, M. *et al.* Hapke modeling of Rhea surface properties through Cassini-VIMS spectra. *Icarus* **214**, 541–555 (2011).
28. De Sanctis, M. C., Capria, M. T. & Coradini, A. Thermal evolution model of 67P/Churyumov-Gerasimenko, the new Rosetta target. *Astron. Astrophys.* **444**, 605–614 (2005).
29. Capria, M. T., Coradini, A., De Sanctis, M. C. & Blecka, M. I. P/Wirtanen thermal evolution: effects due to the presence of an organic component in the refractory material. *Planet. Space Sci.* **49**, 907–918 (2001).
30. JPL Small-Body Database Browser. 67P/Churyumov-Gerasimenko. <http://ssd.jpl.nasa.gov/sbdb.cgi> (NASA/Jet Propulsion Laboratory).

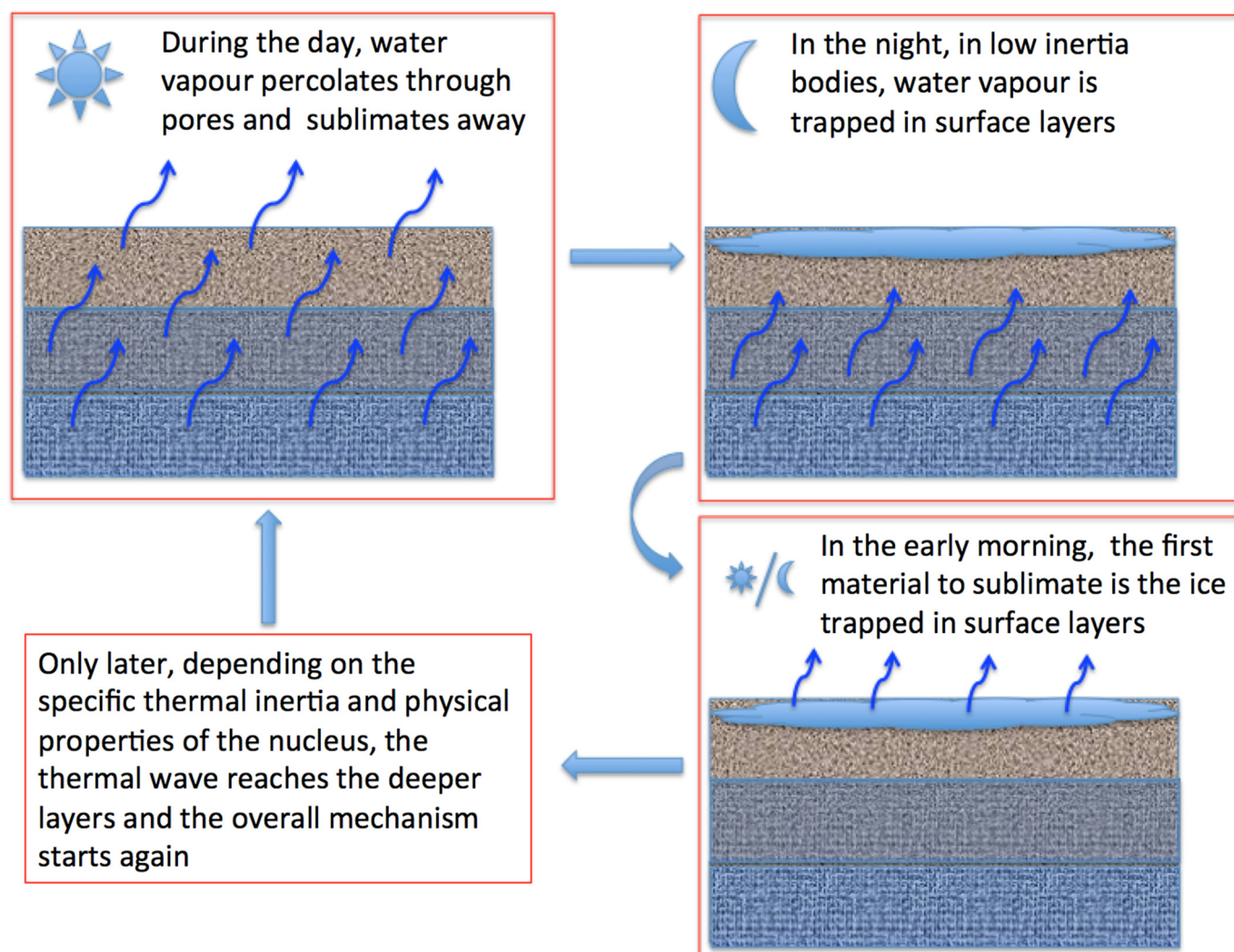


Extended Data Figure 1 | Spectral fit. **a, b**, Two mixing modalities, intimate (**a**) and areal (**b**), are used to model the same spectrum; the spectrum is identified by its position in the acquired image ('sample' and 'line') and its spacecraft event time (scet). The three missing parts of the spectra are related to the wavelength ranges covered by the junctions of the filters which produce significant artefacts. They are thus removed during the fitting procedure. The

spectra are normalized with respect to $\lambda_0 = 1.8 \mu\text{m}$. For the areal mixture case, the modelled absorption band at $2 \mu\text{m}$ is relevant, even with the small abundance ($f_{\text{H}_2\text{O}}$) and grain diameter ($d_{\text{H}_2\text{O}}$) we retrieved. This implies a worse fit, as indicated by the larger χ^2 variable. The intimate mixture is thus a better model of the spectra.

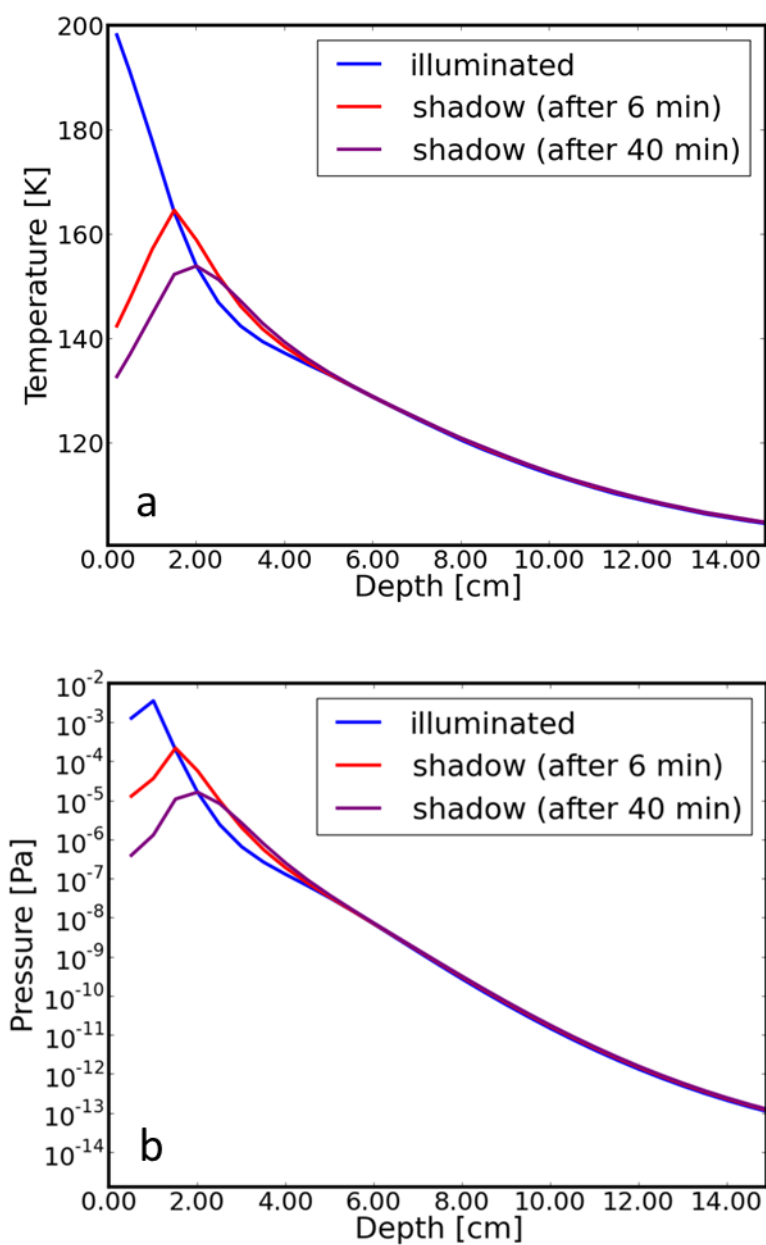


Extended Data Figure 2 | Spectral fits of comet nucleus spectra with different ice content. From a to c, the depth of the absorption band at $3.2 \mu\text{m}$ decreases and the band centre moves slightly towards longer wavelengths. In all cases the spectra are well modelled with a decreasing amount of water ice ($f_{\text{H}_2\text{O}}$) and a constant grain diameter ($d_{\text{H}_2\text{O}}$) of that water ice. Missing parts of the spectra and normalization are as for Extended Data Fig. 1.



Extended Data Figure 3 | Diurnal cycle of water. In the case reported here, the sublimation of water vapour takes place in a deeper layer (see cartoon for a graphic explanation). The water vapour filters up to the surface layers (which are essentially dehydrated, as during the day we do not see any spectral signature of ice) where, finding lower temperature conditions (as in the

night or in the shadow), it condenses and is trapped as ice. The subsequent illumination of the surface leads to absolute loss of the condensed water vapour. This is an effective mechanism of transport of H_2O from deeper layers to the surface.



Extended Data Figure 4 | Temperature and water vapour profiles.

a, Temperature profiles, and **b**, water vapour pressure profiles, from the nucleus surface to the interior at different times: the blue curve is the profile when the

area is illuminated; the red curve is the profile obtained 6 min after passing into shadow; and the purple curve is about 40 min after passing into shadow.

Extended Data Table 1 | Characteristics of VIRTIS observations

FILENAME	II_00369167614.QUB
OBSERVATION START TIME (yyyy-mm-dd hh:mm:ss)	2014-09-12 18:34:43.818
OBSERVATION END TIME (yyyy-mm-dd hh:mm:ss)	2014-09-12 19:10:57.456
SPACECRAFT ALTITUDE	27.849 Km
PHASE ANGLE	63.1 deg
PIXEL RESOLUTION	6.7 m/pix
FILENAME	II_00369210814.QUB
OBSERVATION START TIME (yyyy-mm-dd hh:mm:ss)	2014-09-13 06:34:43.976
OBSERVATION END TIME (yyyy-mm-dd hh:mm:ss)	2014-09-13 07:10:57.604
SPACECRAFT ALTITUDE	28.19 Km
PHASE ANGLE	60.7 deg
PIXEL RESOLUTION	7.1 m/pix
FILENAME	II_00369345274.QUB
OBSERVATION START TIME (yyyy-mm-dd hh:mm:ss)	2014-09-14 19:55:43.981
OBSERVATION END TIME (yyyy-mm-dd hh:mm:ss)	2014-09-14 20:30:57.680
SPACECRAFT ALTITUDE	28.2 Km
PHASE ANGLE	63.6 deg
PIXEL RESOLUTION	7.05 m/pix

Extended Data Table 2 | Main parameters used in the comet model

Physical Quantity	Value	Reference
Rotation Period	12.403 [h]	[12]
Semi-major Axis	3.463 [AU]	[30]
Eccentricity	0.641	[30]
Albedo	0.06	[7]
Emissivity	0.9	[22,24, 28,29]
Dust (Silicates) /Ice	1.5	Adopted for this model and typically used in cometary thermophysical models
Dust (Organics)/Ice	2.0	Adopted for this model and typically used in cometary thermophysical models
Mean Pore Radius	10^{-4} [m]	[22,24]
Porosity	0.6	Adopted for this model and typically used in cometary thermophysical models
Hertz Factor (the area of contact between material grains relative to the cross-sectional area)	0.01	[22,24]
Silicatic Dust Thermal Conductivity	3 [W K ⁻¹ m ⁻¹]	[22,24,29]
Organic Dust Thermal Conductivity	0.25 [W K ⁻¹ m ⁻¹]	[22,24,29]
H ₂ O (crystalline) thermal conductivity	567/T [W K ⁻¹ m ⁻¹]	[22,24,29]
Mean Density	400 [Kg m ⁻³]	Resulting from the parameters used
Thermal Inertia	50-70 [J m ⁻² K ⁻¹ s ^{-0.5}]	Resulting from the parameters used
Initial Temperature	100 [K]	Adopted for this model and typically used in cometary thermophysical models

References are Sierks *et al.*⁷, Mottola *et al.*¹², De Sanctis *et al.*²², De Sanctis *et al.*²⁴, De Sanctis *et al.*²⁸, Capria *et al.*²⁹, JPL Small-Bodies³⁰

References cited in this table are as follows: refs 7, 12, 22, 24, 28, 29, 30.